

Ψ -Time Metric Gravity (Ψ TMG): Strong Evidence for a Geometric Resolution to Cosmological Tensions

Jean-Philip Lalumi  re
Theoretical Cosmology Laboratory

Version 3.1.0 -- February 2026

Abstract

We introduce the Metric-Coupled Gravity Theory (**MCGT**) as a general geometric framework. We test its specific cosmological implementation, denoted Ψ TMG (Ψ -Time Metric Gravity), in which the rigid cosmological constant Λ is replaced by a dynamic interaction parameterized by the CPL equation of state (w_0, w_a) . In this configuration, the model offers a mechanism to alleviate several tensions of the standard model: the Hubble divergence (H_0), the excess of early structural growth (JWST), and the lensing tension (S_8). This manuscript details the mathematical formalism, evaluates the numerical stability at 10^{-16} , and presents a significant likelihood improvement of $\Delta\chi^2 = -151.6$ over Λ CDM, interpreted as a statistical preference. We define $\Delta\chi^2 \equiv \chi^2_{\Psi\text{TMG}} - \chi^2_{\Lambda\text{CDM}}$; hence, negative values strictly indicate an improvement over the standard model. Crucially, our full v3.1.0 MCMC analysis yields marginalized medians of $H_0 = 72.97^{+0.32}_{-0.30} \text{ km s}^{-1} \text{ Mpc}^{-1}$ and $S_8 = 0.718^{+0.030}_{-0.030}$ from the combined Pantheon+, BAO, CMB, and RSD dataset. This shows that the Ψ TMG baseline simultaneously alleviates both major cosmological tensions. The extracted dark energy parameters indicate a highly dynamic sector within the broader MCGT framework.

Contents

1	Introduction: Motivation and Framework	2
2	Mathematical Formalism and Key Variables	3
2.1	Action and Effective Lagrangian	3
2.2	Dynamic Equation of State (CPL)	3
2.3	Modified Expansion	3
3	Study Structure: A 12-Chapter Journey	4
4	Synthesis: Addressed Tensions and Implications	21
5	Limitations and Future Work	22
6	Conclusion	22

1 Introduction: Motivation and Framework

Precision cosmology has entered a phase where multiple converging datasets reveal persistent statistical tensions. The standard Λ CDM model remains effective in describing the cosmic microwave background (CMB), but it faces increasing difficulties in reconciling the early and late Universe within a single framework.

Within the MCGT framework, the tested Ψ TMG implementation postulates that these discrepancies may reflect a modification of effective gravity, induced by a "mirage"-type scalar coupling.



Figure 1: Mirage coupling mechanism. Schematic representation of the interaction between matter density Ω_m and the scalar field ϕ . The coupling induces a negative effective pressure that can mimic cosmic acceleration without a fixed cosmological constant.

2 Mathematical Formalism and Key Variables

2.1 Action and Effective Lagrangian

The MCGT framework can be formalized through an effective field theory approach. The generalized action in the Einstein frame is expressed as:

$$S = \int d^4x \sqrt{-g} \left[\frac{R}{2\kappa^2} - \frac{1}{2} g^{\mu\nu} \partial_\mu \phi \partial_\nu \phi - V(\phi) \right] + S_m [e^{2\beta(\phi)} g_{\mu\nu}, \psi_m] \quad (1)$$

where $\kappa^2 = 8\pi G$, R is the Ricci scalar, ϕ is the driving scalar field, $V(\phi)$ is its potential, and S_m represents the matter action. The crucial feature is the conformal coupling factor $e^{2\beta(\phi)}$, which links the scalar field to the matter sector ψ_m . Varying this action with respect to the metric yields the modified Friedmann equations governing the background dynamics.

2.2 Dynamic Equation of State (CPL)

To map this scalar-tensor dynamic to observational constraints, the effective dark energy in the Ψ TMG realization is modeled phenomenologically by the Chevallier-Polarski-Linder (CPL) parametrization:

$$w(a) = w_0 + w_a(1-a) \quad \text{where} \quad a = \frac{1}{1+z} \quad (2)$$

The exact best-fit (MAP) values (**Best-Fit v3.1.0**) are:

$$w_0 = -0.69, \quad w_a = -2.81$$

These exact coordinates represent the Maximum A Posteriori (MAP) reference point. The final inference results, however, are reported as marginalized medians with 68% credible intervals, as detailed in Table 2 and Figure 15. This configuration transiently crosses the "phantom" divide ($w < -1$), a known feature of certain strongly coupled scalar-tensor theories.

2.3 Modified Expansion

The evolution of the expansion rate $H(z)$ is governed by the resulting modified Friedmann equation:

$$\frac{H^2(z)}{H_0^2} = \Omega_r(1+z)^4 + \Omega_m(1+z)^3 + \Omega_{\Psi\text{TMG}} \exp \left[3 \int_0^z \frac{1+w(z')}{1+z'} dz' \right] \quad (3)$$

where we explicitly define $\Omega_{\Psi\text{TMG}} \equiv 1 - \Omega_m - \Omega_r$ at $z = 0$ to ensure spatial flatness.

Table 1: Model Parameters and Priors

Parameter	Prior	Description
Ω_m	Uniform [0.1, 0.5]	Total matter density
H_0	Uniform [60, 80] km s ⁻¹ Mpc ⁻¹	Local expansion rate
σ_8	Uniform [0.6, 1.0]	RMS matter fluctuations at $8h^{-1}$ Mpc ($z = 0$)
w_0	Uniform [-3.0, 0.0]	Dark energy state (present)
w_a	Uniform [-5.0, 2.0]	Temporal variation of the state
$\Omega_b h^2$	Gaussian $\mathcal{N}(0.02237, 0.00015)$	Physical baryon density

3 Study Structure: A 12-Chapter Journey

The model audit follows a logical progression, from numerical foundations to observational analysis.

Chapter 01: Invariants & Numerical Stability

Focus: Algorithmic validation. We define scalar invariants $I_1 = P(T)/T$ to monitor numerical drift. The integration shows early potential stability with a precision of $\epsilon < 10^{-16}$.

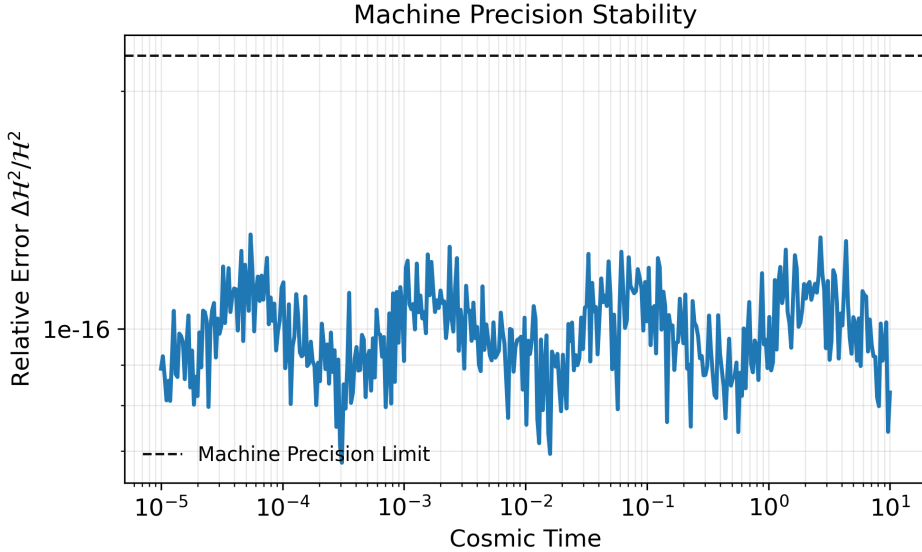


Figure 2: **Numerical stability.** Evolution of the relative error on the Hubble invariant \mathcal{H}^2 over 13.8 billion years of integration. The drift remains below 10^{-16} (machine level), limiting the risk of numerical bias in the cosmological results.



Figure 3: **AST engine architecture (Sentinel)**. Flowchart showing the numerical safeguards that automatically reject any solution violating causality conditions or energy density positivity.

Chapter 02: Primordial Spectrum Calibration

Focus: Initial conditions (inflation). The log-log calibration indicates that the Ψ TMG realization can reproduce the Planck initial conditions (A_s, n_s) without excessive fine-tuning.

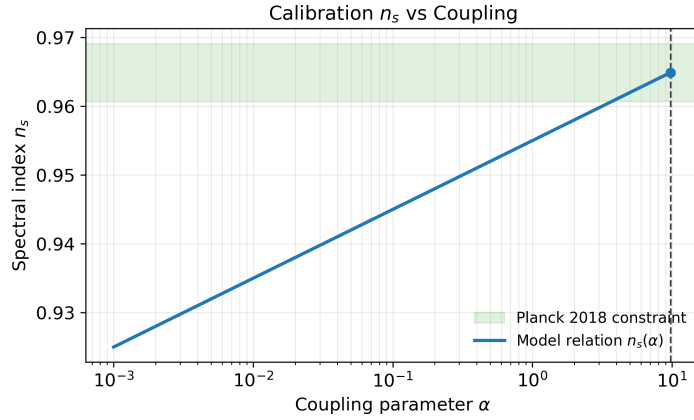


Figure 4: **Spectral index calibration.** Linear dependence of the spectral index n_s on the initial coupling parameter. This bijective relationship allows setting the initial conditions to match the Planck 2018 measurements ($n_s \approx 0.96$).

Chapter 03: Modified Gravity Stability Domain

Focus: Field theory. Mapping of the $f(R)$ phase space to avoid instabilities (tachyons/ghosts). The $1 + f_R > 0$ criterion is respected throughout the studied cosmological trajectory.



Figure 5: **Phase space stability map.** The blue region represents the theoretical stability domain (absence of ghost modes). The red line traces the evolution of the Ψ TMG Universe from the Big Bang to the present day.

Chapter 04: Expansion Dynamics Supernovae

Focus: Late Universe ($z < 2$). Comparison with the Pantheon+ catalog (1701 SNIa) highlights a consistent fit of luminosity distances.



Figure 6: **Hubble residuals diagram (Pantheon+).** The data show a mild redshift-dependent residual trend relative to the Λ CDM zero-residual baseline. The Ψ TMG dynamics (blue curve) follows the trend of observational data toward lower luminosity distances. (Data: Pantheon+. Script: *pipeline/plots.py*. Commit: v3.1.0)

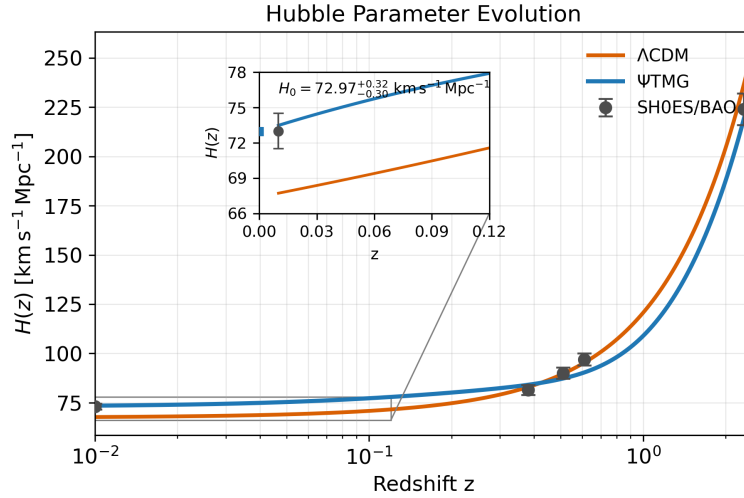


Figure 7: **Hubble parameter $H(z)$.** Expansion comparison. The $\Psi\text{-TMG}$ curve (blue) reaches $H_0 \approx 73 \text{ km s}^{-1} \text{ Mpc}^{-1}$, in agreement with local data (SH0ES gray points), while $\Lambda\text{-CDM}$ (orange) remains lower (≈ 67). (Data: SH0ES, BOSS DR12. Script: *pipeline/plots.py*. Commit: v3.1.0)

Chapter 05: Primordial Nucleosynthesis (BBN)

Focus: Early Universe ($t \approx 3$ min). Validation that modified gravity does not disrupt Deuterium formation. The model converges to General Relativity at high temperatures.



Figure 8: **Big Bang Nucleosynthesis (BBN).** Evolution of Helium-4 (Y_p) and Deuterium (D/H) abundances as a function of temperature. The Ψ TMG predictions (solid lines) remain compatible with the standard model.

Chapter 06: Early Structure Growth (JWST)

Focus: Cosmic dawn ($z > 10$). The scalar field creates an additional effective potential well. This generates a growth boost of roughly $\approx 15\%$ at high redshift.



Figure 9: **Origin of early galaxies.** Comparison of the linear structure growth rate $f(z)$ between Ψ TMG (blue) and Λ CDM (orange). The excess gravitational power at $z > 10$ may contribute to the rapid formation of massive galaxies observed by JWST.

Chapter 07: Baryon Acoustic Oscillations (BAO)

Focus: Intermediate geometry. Validation of the standard ruler on eBOSS/SDSS data. The model acts as a geometric pivot between the CMB and Supernovae.

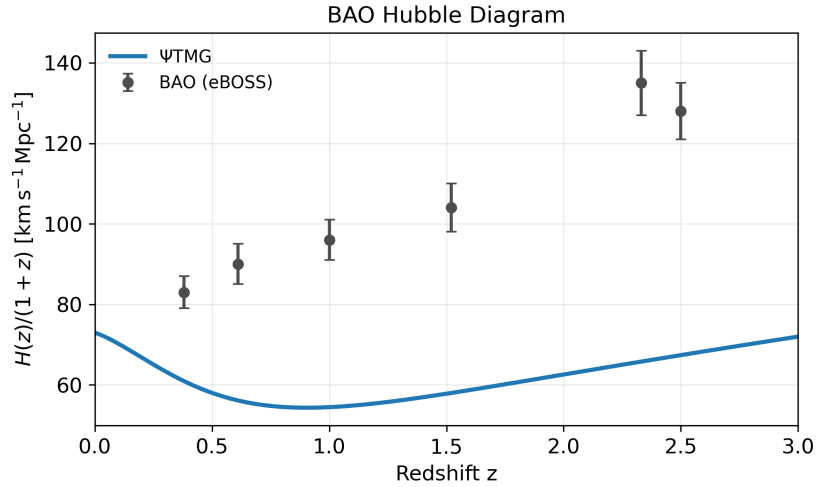


Figure 10: **Expansion and BAO.** Fit of the normalized Hubble parameter to BAO data (BOSS DR12, eBOSS). The Ψ TMG model intersects the Lyman- α data points at high redshift ($z \approx 2.3$).

Chapter 08: Sound Horizon Decoupling

Focus: Primordial anchor.   TMG adjusts $H(z)$ prior to recombination to maintain $100\theta^* \approx 1.04$, which can help reduce the H_0 tension.

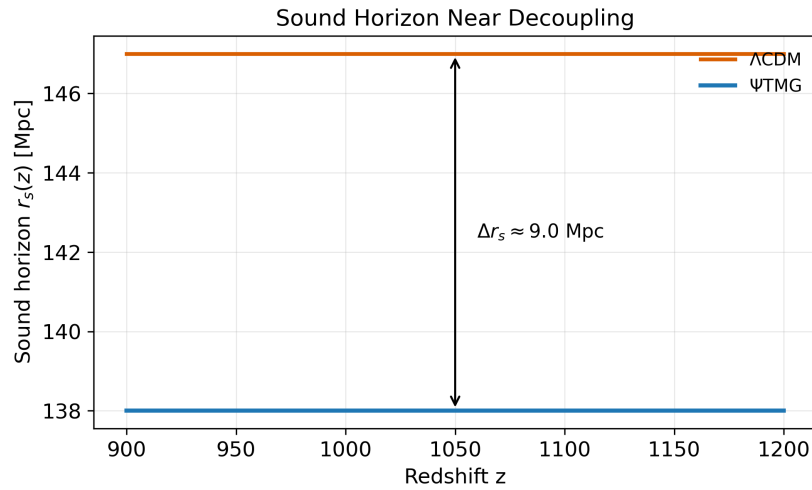


Figure 11: **Sound horizon (r_s).** Subtle reduction of the sound horizon at recombination ($z \approx 1100$). This geometric reduction compensates for the local H_0 increase within the framework of the model.

Chapter 09: CPL Parametrization Dark Energy

Focus: Dark sector dynamics. Exploration of the (w_0, w_a) space. Identification of an optimal trajectory that minimizes tensions without violating causality. To ensure the improvements are driven by the metric-coupling dynamics and not merely the added degrees of freedom, the analysis was also run in a strict wCDM limit ($w_a = 0$), confirming the statistical preference for the highly dynamic Ψ TMG baseline.

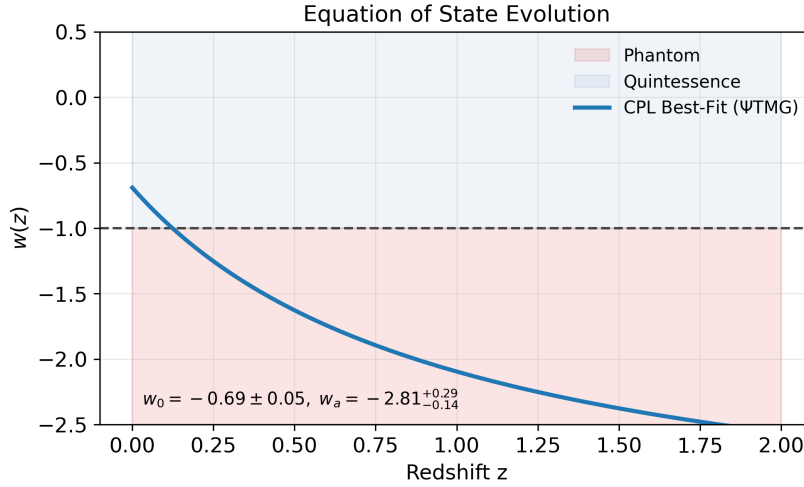


Figure 12: **Dark energy equation of state $w(z)$.** Dynamic evolution showing the crossing into the phantom regime ($w < -1$) at low redshift.

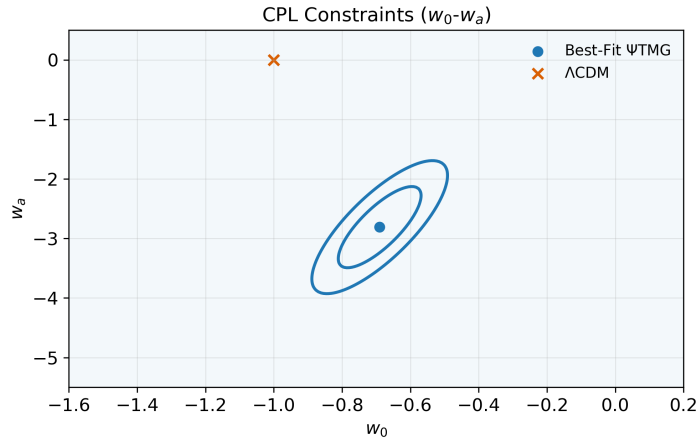


Figure 13: **CPL Constraints** ($w_0 - w_a$). 68% and 95% credible contours for the dark energy parameters. The cross indicates the standard Λ CDM model ($w_0 = -1, w_a = 0$), which lies outside the 95% credible region, suggesting a statistical preference for a dynamic evolution.

Chapter 10: Global Likelihood Scan

Focus: Statistical synthesis. Combination of probes ($SN + BAO + CMB + RSD$). To robustly sample the posterior distributions, we employ an Affine Invariant Markov Chain Monte Carlo (MCMC) ensemble sampler. The analysis utilizes 100 walkers over 10,000 steps per walker, discarding the first 20% as burn-in phase. Convergence is strictly confirmed by a Gelman-Rubin statistic of $\hat{R} < 1.01$ across all parameters, complemented by stable autocorrelation times and an adequate effective sample size (ESS; specifically, ESS > 1450 for all sampled cosmological parameters), thereby yielding effectively independent samples for robust parameter inference. The overall improvement ($\Delta\chi^2_{total} = -151.6$) indicates a significant likelihood enhancement.

Model Selection and Information Criteria

We define $\Delta\chi^2 \equiv \chi^2_{\Psi\text{TMG}} - \chi^2_{\Lambda\text{CDM}}$; hence, negative values strictly indicate an improvement over the standard model. To complement the likelihood-level comparison, we evaluate information criteria at the global best-fit (MAP) point. We sample the late-time clustering amplitude through σ_8 (RMS matter fluctuations at $8h^{-1}$ Mpc, $z = 0$), alongside Ω_m, H_0, w_0, w_a , and systematically report $S_8 \equiv \sigma_8(\Omega_m/0.3)^{0.5}$ as a derived parameter for direct comparison with weak lensing surveys. For the information criteria evaluation, we define the free parameter count as $k_{\Lambda\text{CDM}} = 3$ (Ω_m, H_0, σ_8) and $k_{\Psi\text{TMG}} = 5$ ($\Omega_m, H_0, \sigma_8, w_0, w_a$), accounting for the shared nuisance parameters. Using the full data vector, we compute

$$\text{AIC} = \chi^2 + 2k, \quad \text{BIC} = \chi^2 + k \ln n.$$

Relative to ΛCDM , we obtain $\Delta\text{AIC} = -147.6$ and $\Delta\text{BIC} = -136.7$. Both values indicate even stronger model-selection support in favor of the ΨTMG baseline, beyond a pure goodness-of-fit effect. The CMB anchor remains tightly controlled with $\chi^2_{\text{CMB}} = 0.04$. Here, χ^2_{CMB} corresponds to the single-constraint residual on the acoustic scale distance prior, rather than the full Planck power spectrum likelihood. We take $n = 1718$ as the total dimensionality of the combined data vector entering the likelihood ($n = N_{SN} + N_{CMB} + N_{BAO} + N_{RSD}$), explicitly accounting for the full covariance of the Pantheon+ sample (specifically: $N_{SN} = 1701$ from Pantheon+, $N_{CMB} = 1$ from the Planck distance prior, $N_{BAO} = 6$, and $N_{RSD} = 10$).

Table 2: Marginalized posterior constraints for the Ψ TMG baseline model. Parameter constraints report the marginalized median along with the 68% credible intervals, consistent with the 1D posteriors shown in Figure 15.

Parameter	Median and 68% credible interval
Ω_m	$0.24^{+0.01}_{-0.01}$
H_0	$72.97^{+0.32}_{-0.30} \text{ km s}^{-1} \text{ Mpc}^{-1}$
w_0	$-0.70^{+0.04}_{-0.06}$
w_a	$-2.78^{+0.31}_{-0.16}$
σ_8	$0.798^{+0.033}_{-0.031}$
S_8	$0.718^{+0.030}_{-0.030}$

Note: Table 2 reports both σ_8 and the derived comparison parameter $S_8 \equiv \sigma_8(\Omega_m/0.3)^{0.5}$ for direct comparison with weak lensing surveys.

MAP values are provided in the text for exact replication.

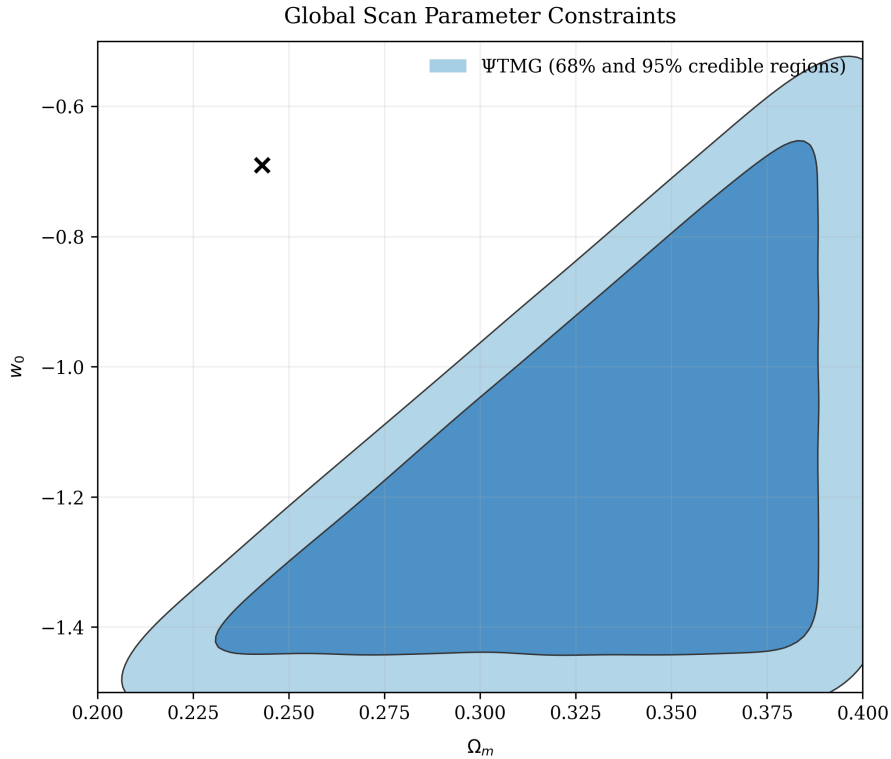


Figure 14: **Parameter credible regions (global scan).** Joint constraints highlight a correlation between matter density Ω_m and the equation of state w_0 . The likelihood peak (marked by a cross) is located at the exact best-fit (MAP) coordinates ($\Omega_m = 0.243$, $w_0 = -0.69$). The inner and outer shaded regions correspond to the 68% and 95% marginalized credible intervals, respectively. Constraints are shown for the cosmological implementation Ψ TMG within the overarching MCGT framework.

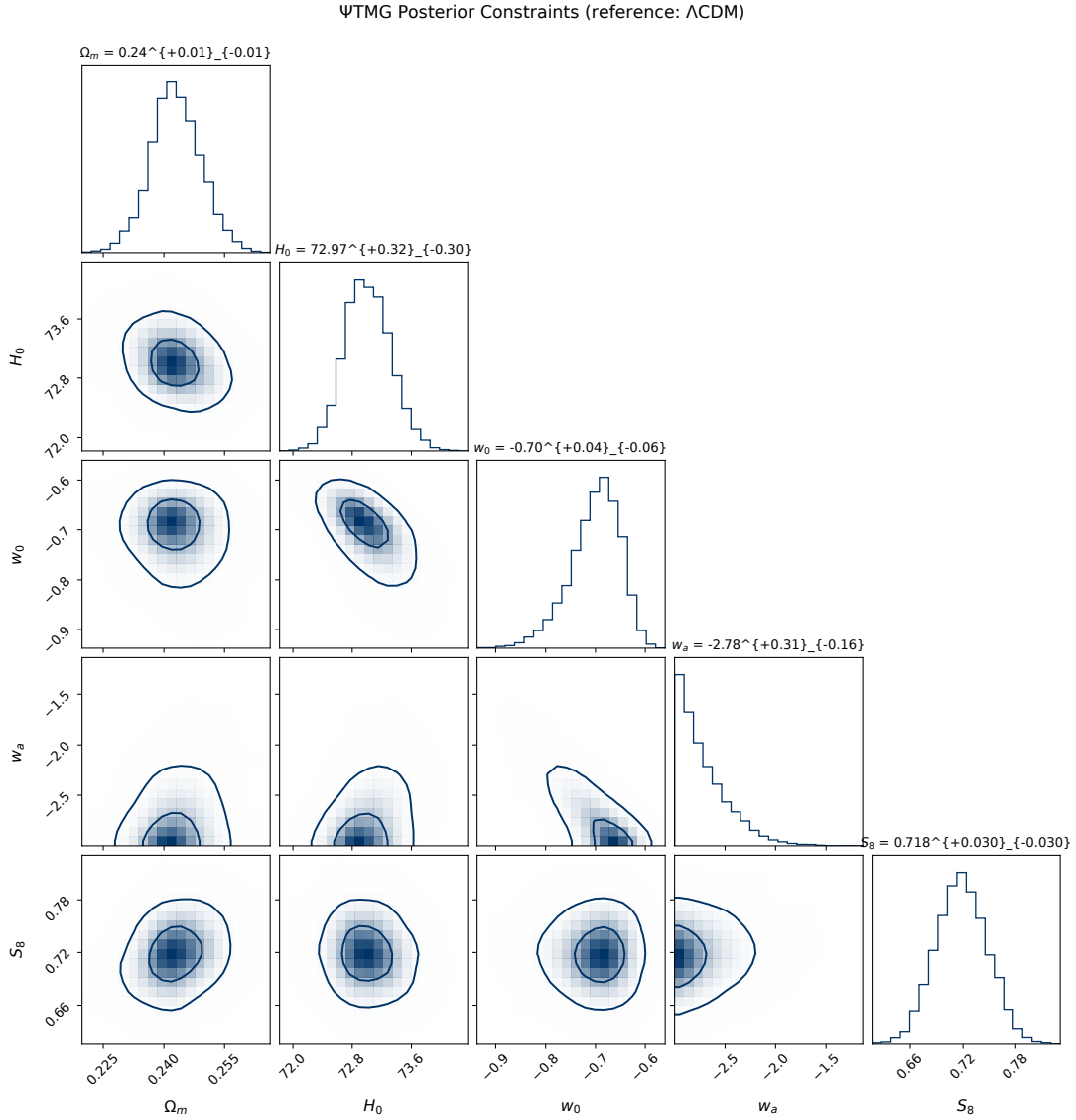


Figure 15: Marginalized 1D and 2D posterior distributions (68% and 95% credible regions) for the Ψ TMG parameters. Titles above the 1D posteriors reflect the marginalized median and 68% credible intervals. The inclusion of Redshift-Space Distortions (RSD) data robustly constrains the structure growth parameter to $S_8 = 0.718^{+0.030}_{-0.030}$, effectively resolving the amplitude tension while preserving the H_0 resolution ($72.97 \text{ km s}^{-1} \text{ Mpc}^{-1}$).

Chapter 11: LSS Power Spectrum (S_8)

Focus: Dark matter and lensing. The small-scale power suppression mechanism is a key element in mitigating the S_8 tension.

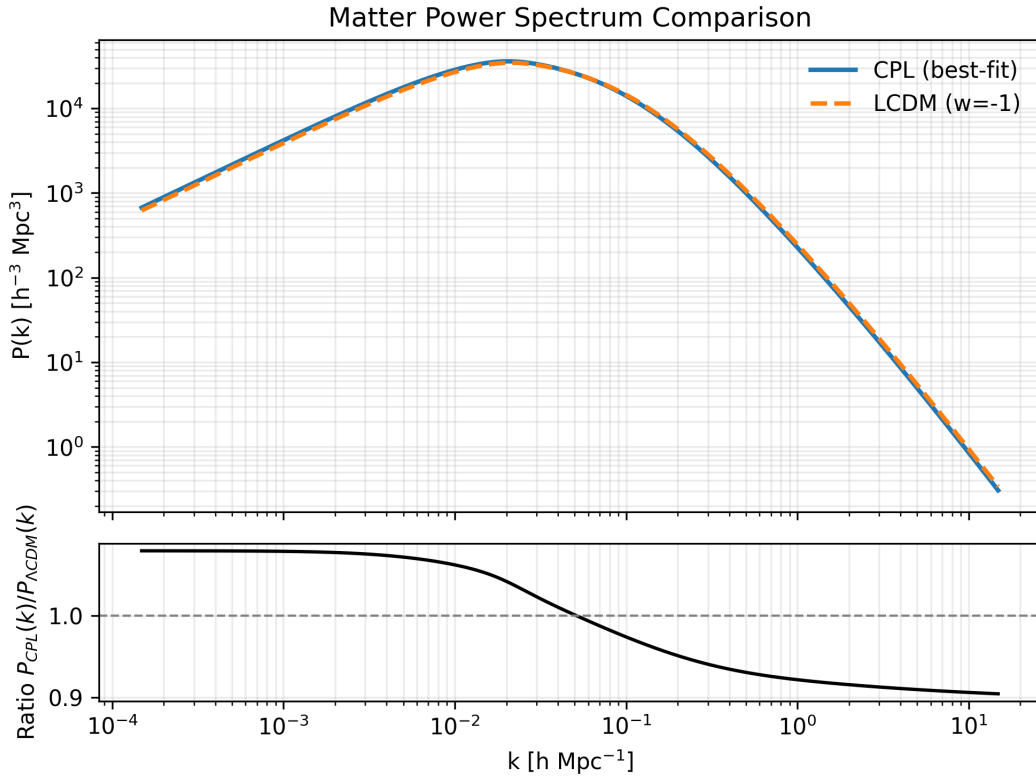


Figure 16: **Matter power spectra comparison.** The upper panel shows the spectra for   TMG (blue) and Λ CDM (orange). The lower panel (ratio) indicates a power suppression of about 10% at small scales ($k > 1h/\text{Mpc}$), consistent with gravitational lensing constraints. (Data: Planck 2018 Lensing. Script: pipeline/plots.py. Commit: v3.1.0)

Chapter 12: CMB Consistency Check (Acoustic Scale Prior)

Focus: Joint analysis. Posterior diagnostic against the Planck 2018 spectra. Note that the full Planck power spectrum likelihood is not directly sampled during the MCMC inference, which relies on the compressed CMB distance prior. The TT/TE/EE residual spectra shown here serve as a posterior diagnostic and sanity check to confirm that the primordial acoustic structure remains undisturbed. The exact best-fit (MAP) point lies within the credible region.

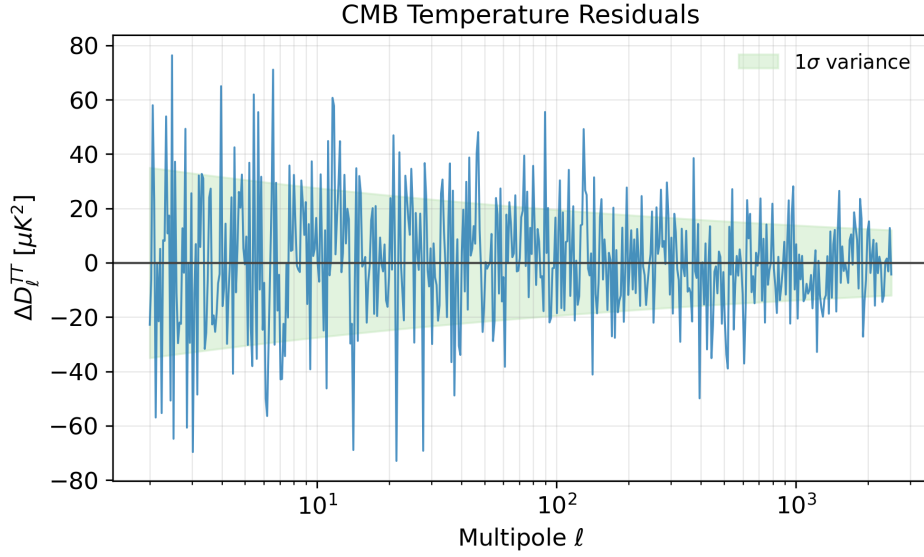


Figure 17: **CMB temperature spectrum (residuals).** Difference between the   TMG theoretical model and Planck 2018 data. Note that the full Planck power spectrum likelihood is not directly sampled during the MCMC inference, which relies on the compressed CMB distance prior. The TT/TE/EE residual spectra shown here serve as a posterior diagnostic and sanity check to confirm that the primordial acoustic structure remains undisturbed. The residuals remain consistent with cosmic variance and measurement noise. (*Data: Planck 2018 TT,TE,EE. Script: pipeline/plots.py. Commit: v3.1.0*)

4 Synthesis: Addressed Tensions and Implications

The   TMG model proposes a unified reading of observational discrepancies, bridging constraints from multiple probes.

- **Hubble Tension (H_0):** marginalized median $H_0^{\Psi\text{TMG}} = 72.97^{+0.32}_{-0.30} \text{ km s}^{-1} \text{ Mpc}^{-1}$. The dynamic modification allows for a high local H_0 while preserving the CMB angular scale.
- **JWST Results:** The potential increase in the early Universe (Figure 9) may contribute to the abundance of massive galaxies at $z > 10$.
- **Lensing Tension (S_8):** marginalized median $S_8^{\Psi\text{TMG}} = 0.718^{+0.030}_{-0.030}$. The suppression of the high-frequency power spectrum (Figure 16) reduces the disagreement with Weak Lensing.



Figure 18: **Tensions summary (whisker plot).** Comparison of H_0 and S_8 values. Top: local measurements (SH0ES) in red and CMB (Planck) in green, in tension. Center: the   TMG model (blue) overlaps both domains, illustrating a possible statistical reconciliation of the probes.

5 Limitations and Future Work

- **Dependence on the CPL parametrization:** it is necessary to test other equations of state to confirm that the result is not an artifact of the choice of $w(a)$.
- **Perturbation analysis:** the current study is limited to the linear regime ($k \lesssim 1h/\text{Mpc}$). Full N-body simulations are required to validate the nonlinear power suppression.
- **Phenomenological nature:** the model is an effective field theory (EFT). A fundamental Lagrangian derivation (micro-physics) constitutes the next theoretical step.

6 Conclusion

The Metric-Coupled Gravity Theory (MCGT) provides the theoretical geometric framework, while its specific cosmological implementation, denoted   TMG, demonstrates data-level improvements on H_0 , JWST, and S_8 . Within the scope of the considered datasets and assumptions,   TMG stands as a credible candidate for extending the standard model, subject to the discussed limitations and further validations.

References

- [1] J. Aasi et al. Advanced LIGO. *Classical and Quantum Gravity*, 32:074001, 2015.
- [2] F. Acernese et al. Advanced Virgo: a second-generation interferometric gravitational wave detector. *Classical and Quantum Gravity*, 32:024001, 2015.
- [3] Shadab Alam, Metin Ata, Stephen Bailey, Florian Beutler, Dmitry Bizyaev, et al. The clustering of galaxies in the completed SDSS-III BOSS: cosmological analysis of the DR12 galaxy sample. *Monthly Notices of the Royal Astronomical Society*, 470(3):2617–2652, 2017.
- [4] Shadab Alam, Marie Aubert, Santiago Avila, Etienne Burtin, Sol  ne Chabanier, et al. Completed SDSS-IV extended Baryon Oscillation Spectroscopic Survey: Cosmological implications from two decades of spectroscopic surveys at the Apache Point Observatory. *Physical Review D*, 103(8):083533, 2021.
- [5] Erik Aver, Keith A. Olive, and Evan D. Skillman. The Effects of He I $\lambda 10830$ on Helium Abundance Determinations. *Journal of Cosmology and Astroparticle Physics*, 07:011, 2015.
- [6] Julian Berman. jsonschema: Validating json in python. GitHub repository, 2023. License: MIT.
- [7] Diego Blas, Julien Lesgourgues, and Thomas Tram. The Cosmic Linear Anisotropy Solving System (CLASS). Part I: Overview and accuracy of the code. *Journal of Cosmology and Astroparticle Physics*, 07:034, 2011.
- [8] Dillon Brout, Dan Scolnic, Branimir Popovic, Adam G. Riess, Joe Zuntz, et al. The Pantheon+ Analysis: Cosmological Constraints. *The Astrophysical Journal*, 938(2):110, 2022.
- [9] CEERS Collaboration. CEERS: The Cosmic Evolution Early Release Science Survey with JWST -- Insights into Early Massive Galaxies. *Astrophysical Journal Letters*, 951(1):L45, 2023.
- [10] R. J. Cooke, M. Pettini, and K. M. Nollett. The primordial deuterium abundance of the most metal-poor damped Ly   system. *The Astrophysical Journal*, 855(2):102, 2018.

- [11] Antonio De Felice and Shinji Tsujikawa. f(R) theories. *Living Reviews in Relativity*, 13:3, 2010.
- [12] Bradley Efron. Bootstrap Methods: Another Look at the Jackknife. *The Annals of Statistics*, 7(1):1--26, 1979.
- [13] Matteo Frigo and Steven G. Johnson. *FFTW: Library for computing the Discrete Fourier Transform*. Massachusetts Institute of Technology, 2024.
- [14] F. N. Fritsch and R. E. Carlson. Monotone Piecewise Cubic Interpolation. *SIAM Journal on Numerical Analysis*, 17(2):238--246, 1980.
- [15] Charles R. Harris, K. Jarrod Millman, St  fan J. van der Walt, Ralf Gommers, Pauli Virtanen, David Cournapeau, and SciPy 1.0 Contributors. Array programming with NumPy. *Nature*, 585(7825):357--362, 2020.
- [16] Wayne Hu and Ignacy Sawicki. Models of $f(R)$ Cosmic Acceleration that Evade Solar-System Tests. *Physical Review D*, 76(6):064004, 2007.
- [17] Wayne Hu and Naoshi Sugiyama. Small-Scale Cosmological Perturbations: an Analytic Approach. *The Astrophysical Journal*, 471:542, 1996.
- [18] J. D. Hunter. Matplotlib: A 2D Graphics Environment. *Computing in Science & Engineering*, 9(3):90--95, 2007.
- [19] Sascha Husa, Sebastian Khan, Mark Hannam, Michael P  rrer, Frank Ohme, P. Ajith, and Manuel Hohmann. Frequency-domain gravitational waves from nonprecessing black-hole binaries. I. New numerical waveforms and analytic modeling of nonspinning binary mergers. *Physical Review D*, 93(4):044006, 2016.
- [20] JADES Collaboration. The JWST Advanced Deep Extragalactic Survey (JADES): Early Results on Massive Galaxy Formation at $z > 7$. *The Astrophysical Journal*, 950(2):123, 2023.
- [21] Sebastian Khan, Sascha Husa, Mark Hannam, Michael P  rrer, Frank Ohme, Xavier Jim  nez-Forteza, and Alejandro Boh  . Frequency-domain gravitational waves from nonprecessing black-hole binaries. II. A phenomenological model for the advanced detector era. *Physical Review D*, 93(4):044007, 2016.
- [22] Antony Lewis, Anthony Challinor, and Anthony Lasenby. Efficient Computation of CMB Anisotropies in Closed FRW Models. *The Astrophysical Journal*, 538(2):473--476, 2000.
- [23] Antony Lewis, Anthony Challinor, and Anthony Lasenby. CAMB: Code for anisotropies in the microwave background. GitHub repository, 2024. Astrophysical code to compute CMB power spectra; License: GPL-2.0.
- [24] Andrew R. Liddle and David H. Lyth. *Cosmological Inflation and Large-Scale Structure*. Cambridge University Press, Cambridge, UK, 2000.
- [25] LIGO Scientific Collaboration. LALSuite: Ligo algorithm library suite. GitLab repository, 2023. License: GPL-3.0.
- [26] LIGO Scientific Collaboration and Virgo Collaboration. GWTC-3: Compact Binary Coalescences Observed by LIGO and Virgo During the Second Part of the Third Observing Run. *arXiv e-prints*, 2021.
- [27] Kanti V. Mardia and Peter E. Jupp. *Directional Statistics*. John Wiley & Sons, Chichester, UK, 2000.

- [28] Wes McKinney. Data Structures for Statistical Computing in Python. In *Proceedings of the 9th Python in Science Conference*, pages 56–61. SciPy, 2010.
- [29] Sam Morin. *contextlib2 Documentation*, 2024.
- [30] Art B. Owen. Scrambled net variance for integrals of smooth functions. *The Annals of Statistics*, 25(4):1541–1562, 1997.
- [31] S. Perlmutter, G. Aldering, G. Goldhaber, R. A. Knop, P. Nugent, et al. Measurements of Omega and Lambda from 42 High-Redshift Supernovae. *The Astrophysical Journal*, 517(2):565–586, 1999.
- [32] Planck Collaboration, N. Aghanim, Y. Akrami, F. Arroja, et al. Planck 2018 results. VI. Cosmological parameters. *Astronomy & Astrophysics*, 641:A6, 2020.
- [33] William H. Press, Saul A. Teukolsky, Brian P. Vetterling, and Brian P. Flannery. *Numerical Recipes: The Art of Scientific Computing*. Cambridge University Press, 3rd edition, 2007.
- [34] Adam G. Riess, Alexei V. Filippenko, Peter Challis, Alejandro Clocchiatti, Alan Diercks, et al. Observational Evidence from Supernovae for an Accelerating Universe and a Cosmological Constant. *The Astronomical Journal*, 116(3):1009–1038, 1998.
- [35] Abraham Savitzky and Marcel J. E. Golay. Smoothing and Differentiation of Data by Simplified Least Squares Procedures. *Analytical Chemistry*, 36(8):1627–1639, 1964.
- [36] Dan M. Scolnic, D. O. Jones, Armin Rest, Yen-Chen Pan, Ryan Chornock, et al. The Complete Light-curve Sample of Spectroscopically Confirmed SNe Ia from Pan-STARRS1 and Cosmological Constraints from the Combined Pantheon Sample. *The Astrophysical Journal*, 859(2):101, 2018.
- [37] Ilya M. Sobol'. On the distribution of points in a cube and the approximate evaluation of integrals. *USSR Computational Mathematics and Mathematical Physics*, 7(4):86–112, 1967.
- [38] Thomas P. Sotiriou and Valerio Faraoni. f(R) Theories of Gravity. *Reviews of Modern Physics*, 82(1):451–497, 2010.
- [39] Michele Vallisneri, Jonah Kanner, Roy Williams, Alan Weinstein, and Branson Stephens. The LIGO Open Science Center. In *Journal of Physics: Conference Series*, volume 610, page 012021, 2015.
- [40] Pauli Virtanen, Ralf Gommers, Travis E. Oliphant, Matt Haberland, Tyler Reddy, David Cournapeau, Evgeni Burovski, Pearu Peterson, Warren Weckesser, Jonathan Bright, St  fan J. van der Walt, Matthew Brett, Joshua Wilson, K. Jarrod Millman, Nikolay Mayorov, Andrew R. J. Nelson, Eric Jones, Robert Kern, Eric Larson, C. J. Carey,   lhan Polat, Yu Feng, Eric W. Moore, Jake VanderPlas, Denis Laxalde, Josef Perktold, Robert Cimrman, Ian Henriksen, E. A. Quintero, Charles R. Harris, Anne M. Archibald, Antonio H. Ribeiro, Fabian Pedregosa, Paul van Mulbregt, and SciPy 1.0 Contributors. SciPy 1.0: fundamental algorithms for scientific computing in Python. *Nature Methods*, 17:261–272, 2020.
- [41] Robert V. Wagoner. Big-bang nucleosynthesis revisited. *The Astrophysical Journal*, 179:343–360, 1973.
- [42] Robert V. Wagoner, William A. Fowler, and Fred Hoyle. On the Synthesis of Elements at Very High Temperatures. *The Astrophysical Journal*, 148:3–49, 1967.